An Analytical Error Model for Spaceborne SAR Multichannel Azimuth Reconstruction

F. Q. de Almeida, M. Younis, G. Krieger, A. Moreira

German Aerospace Center (DLR), Microwaves and Radar Institute
Muenchner Strasse 20, 82234 Wessling, Germany
email: felipe.queirozdealmeida@dlr.de

Keywords: Synthetic Aperture Radar (SAR), High Resolution Wide Swath (HRWS), Digital Beamforming (DBF), Azimuth Beamforming, Error Modelling.

Abstract

In the context of spaceborne synthetic aperture radar (SAR) for remote sensing, multichannel system architectures coupled with digital beamforming techniques are deemed a necessary technological advancement to fulfil the requirements for near future radar missions. Calibration of such systems is an important topic, since channel imbalances may lead to considerable degradation of performance. This paper analyses the impact of residual errors in a SAR system with multiple channels in azimuth and derives an analytical model for the resulting performance degradation, which may be used in system design as an aid to establish requirements in an error budget analysis.

1. Introduction

Spaceborne synthetic aperture radar (SAR) [1], [2] data currently enjoy an increasing acceptance in the scientific community, owing to its myriad applications. Imaging a wide swath with a high spatial resolution (HRWS) [3], [4] – which is necessary to provide a broad and up-to-date coverage of high quality data – is however a fundamental problem in SAR system design [1], since single channel systems are subject to a well-known compromise between azimuth resolution and coverage [5].

The usage of multichannel architectures and digital beamforming (DBF) techniques [6], [7], [8] poses a promising solution to this dilemma and is currently subject of technological development for implementation of a HRWS satellite mission [9], intended as a follow-up for ESA's Sentinel-1. A basic block diagram for the concept, which is based on multichannel sampling [10], [11], is provided in Figure 1.

The signal processing for this class of system relies however in the knowledge of the receive channels' transfer functions [8], which makes adequate channel calibration crucial, as channel imbalances may severely degrade performance [12]. In terms of system design, this poses the problem of how to specify calibration accuracy requirements, which in turn requires an understanding of the impact of such errors over performance. This paper analyses the impact of residual (i.e. post-calibration) channel imbalances on the processing of a system with multiple channels on receive and derives an analytical model for the degradation of the performance in comparison to what is expected in the error-free scenario. Section 2 provides the signal model and mathematical derivation, whereas Section 3 presents simulation results to validate the established model. Finally, Section 4 provides a discussion of the material.

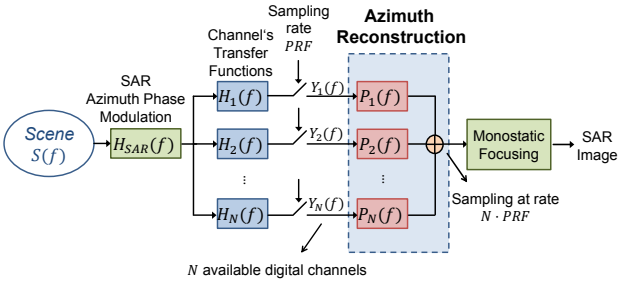

Figure 1: Block diagram for multichannel system in azimuth. The scene's backscattering signal is acquired by N azimuth channels, modelled by their transfer functions $H_k(f)$, at a (typically sub-Nyquist) rate of PRF and the signal processing (digital filters $P_k(f)$ applied on $Y_k(f)$) restores sampling to $N \cdot PRF$, so monostatic focusing yields a SAR image equivalent to a single-channel system sampled directly at $N \cdot PRF$.

2. Multichannel Azimuth Reconstruction and the Effect of Channel Imbalances

2.1 Signal Model: Error-free Case

In the following, a system with one Tx and N Rx azimuth channels is considered. As described in [8] in detail, if the sampling of each of the individual channels occurs at a rate of f_{PRF}, the effective sampling of the equivalent monostatic system is $N \cdot f_{PRF}$, as N samples are recorded for each received pulse. Thus, a complex signal spectrum $U(f)$ of Doppler bandwidth $B_D \leq N \cdot f_{PRF}$ may be recovered unambiguously by proper combination of the aliased spectra of each of the channels in frequency domain.

Taking the limit case, the total signal bandwidth of $N \cdot f_{PRF}$ is divided into N contiguous sub-bands I_m of length f_{PRF}, the first of which is $I_1 = [-N \cdot \frac{f_{PRF}}{2}, -N \cdot \frac{f_{PRF}}{2} + f_{PRF}]$, so that $I_m = I_1 + (m-1) \cdot f_{PRF}$, $1 \leq m \leq N$. Due to the aliasing, the signal spectrum of the channels may be represented in any interval of length f_{PRF}, taken here to be I_1. The k-th azimuth

channel is considered to be described by the transfer function $H_k(f)$, with frequency support in $[-N \cdot \frac{f_{PRF}}{2}, N \cdot \frac{f_{PRF}}{2}]$, and following the sub-band division may also be described for the frequency support of I_1 by $H_k(f + (m-1) \cdot f_{PRF})$, with $1 \leq m, k \leq N$. The complete spectrum $U(f)$ of the scene to be recovered may be divided following the sub-band convention into N signals of bandwidth f_{PRF}, so that $S_m(f) = U(f + (m-1) \cdot f_{PRF})$, for f in I_1, $1 \leq m \leq N$. These signals can be regarded as azimuth *looks* of the SAR image, in accordance with typical SAR processing nomenclature.

Considering that the *k*-th azimuth channel is positioned at Δx_k, and that the platform velocity in along-track is V_P, the channel transfer function in frequency domain after a Taylor expansion may be approximated by [8]

$$H_k(f) = e^{-j \cdot \Delta\phi_k} \cdot e^{-j \cdot 2 \cdot \pi \cdot \Delta t_k \cdot f}, \quad (1)$$

where $\Delta t_k = \frac{\Delta x_k}{2 \cdot V_P}$ are the delays induced by the phase center baselines and $\Delta\phi_k$ is a constant phase.

Taking into account the sub-band division, the multichannel system in frequency domain may be described by the *N x N* matrix $\boldsymbol{H}(f)$ with elements $H_{kl}(f) = H_k(f + (l-1) \cdot f_{PRF})$ and the sub-sampled signal at each channel *k* by

$$Y_k\ (f) = \sum_{m=1}^{N} H_k(f + (m-1) \cdot f_{PRF})\ \cdot S_m(f), \quad (2)$$

so that, in matrix notation,

$$\begin{bmatrix} Y_1\ (f) \\ Y_2\ (f) \\ \vdots \\ Y_N\ (f) \end{bmatrix}_{Nx1} = \boldsymbol{H}(f)_{NxN} \cdot \begin{bmatrix} S_1(f) \\ S_2(f) \\ \vdots \\ S_N(f) \end{bmatrix}_{Nx1}, \quad (3)$$

$\boldsymbol{Y}(f)_{Nx1} = \boldsymbol{H}(f)_{NxN} \cdot \boldsymbol{S}(f)_{Nx1}$.

Reconstruction can be regarded as an estimator

$$\widehat{\boldsymbol{S}}(f)_{Nx1} = \boldsymbol{P}(f)_{NxN} \cdot \boldsymbol{Y}(f)_{Nx1}, \quad (4)$$

where the filter matrix has elements

$$P_{mk}(f) = P_k(f + (m-1) \cdot f_{PRF}) \quad (5)$$

and hence each *look* $S_m(f)$ is recovered by means of row m of matrix $\boldsymbol{P}(f)$, and each column of it is applied to a particular channel k. In particular, $\boldsymbol{P}(f) = \boldsymbol{H}(f)^{-1}$ yields ideal reconstruction of the bandlimited signal in the noiseless case and can be shown to be optimal in a MSE sense even in the presence of noise and a non-bandlimited spectrum [13], [14]. Alternative reconstruction schemes are analyzed in [14], [15].

2.2 Error Model

The signal model in Section 2.1 may be augmented to encompass residual channel errors by considering that the system is actually described by a channel matrix $\boldsymbol{H_{error}}(f)$ which differs from the nominal channel matrix $\boldsymbol{H}(f)$. Thus a modelling error is assumed, which may be caused by residual channel imbalances.

Let each of the *N* channels be affected by a phase error ξ_i, and an amplitude error ϵ_i, $1 \leq i \leq N$. We assume ξ_i to be independent identically distributed (i.i.d.) random values following a uniform distribution in the interval $\left[-\frac{\xi_u}{2}, \frac{\xi_u}{2}\right]$, whereas ϵ_i are i.i.d Gaussian random variables with a distribution $N(0, \sigma_\epsilon^2)$. Furthermore, the amplitude and phase errors are assumed to be independent from each other and from the signal. Then, the actual system matrix becomes

$$\boldsymbol{H_{error}}(f) = \boldsymbol{D} \cdot\ \boldsymbol{H}(f) \quad (6)$$

where the diagonal, frequency independent error matrix has elements

$$\boldsymbol{D} = \mathrm{diag}(1 + \epsilon_i) \cdot \mathrm{diag}(\exp(j \cdot \xi_i)), \quad (7)$$

for $1 \leq i \leq N$.

Reconstruction (cf. (4)) of the signal from the system described by (6) with the nominal reconstruction filters $\boldsymbol{P}(f) = \boldsymbol{H}(f)^{-1}$ yields

$$\widehat{\boldsymbol{S}}(f)_{Nx1} = \boldsymbol{P}(f) \cdot \big(\boldsymbol{D} \cdot \boldsymbol{H}(f)\big) \cdot \boldsymbol{S}(f), \quad (8)$$

or, by expressing $\boldsymbol{D} = \boldsymbol{I} + (\boldsymbol{D} - \boldsymbol{I})$,

$$\widehat{\boldsymbol{S}}(f)_{Nx1} = \boldsymbol{S}(f) + \boldsymbol{P}(f) \cdot (\boldsymbol{D} - \boldsymbol{I}) \cdot \boldsymbol{H}(f) \cdot \boldsymbol{S}(f). \quad (9)$$

The underlying assumption in (9) is namely that the signal can be perfectly reconstructed in the absence of errors, which requires a noise-free band-limited input signal. In practice, this assumption may be reexamined to

$$\widehat{\boldsymbol{S}}(f)_{Nx1} = \boldsymbol{S}_{error-free}(f) + \boldsymbol{P}(f) \cdot (\boldsymbol{D} - \boldsymbol{I}) \cdot \boldsymbol{H}(f) \cdot \boldsymbol{S}(f), \quad (10)$$

where $\boldsymbol{S}_{error-free}(f) \neq \boldsymbol{S}(f)$ is not necessarily the perfectly reconstructed signal. Due to the assumption that the errors are independent of the signal (and also possible of additive noise), the ambiguous power due to them simple adds to that due to other factors such as the excess bandwidth, for instance. The average signal power remains the same, so the final Azimuth Ambiguity-to-Signal Ratio (AASR) in the presence of errors following the model described in this section is

$$AASR = AASR_{error-free} + AASR_{errors}, \quad (11)$$

i.e. an additive term degrading the error-free result obtained for a particular configuration.

2.3 Derivation of Residual Ambiguity Level due to Errors

Defining the reconstruction error as $\boldsymbol{\Delta S}(f) = \widehat{\boldsymbol{S}}(f) - \boldsymbol{S}(f)$, (cf. (9)) the quantity of interest is the residual ambiguous power caused by the errors, that is $\sigma_{error}^2 = E[\|\boldsymbol{\Delta S}(f)\|^2]$. For this, we consider the covariance matrix of the reconstruction error, $E[\boldsymbol{\Delta S}(f) \cdot \boldsymbol{\Delta S^H}(f)]$, whose trace is the residual power in question.

For notational convenience, let the error-free aliased signal be expressed by $\boldsymbol{Y}(f)_{Nx1} = \boldsymbol{H}(f) \cdot \boldsymbol{S}(f)$ and the frequency dependency be dropped by now. One may write

$$\sigma_{error}^2 = \boldsymbol{P} \cdot E[(\boldsymbol{D} - \boldsymbol{I}) \cdot \boldsymbol{Y} \cdot \boldsymbol{Y}^H \cdot (\boldsymbol{D} - \boldsymbol{I})^H] \cdot \boldsymbol{P}^H. \quad (12)$$

The matrix $\boldsymbol{Y} \cdot \boldsymbol{Y^H}$ has elements $Y_i \cdot Y_l^*$, $1 \leq i, l \leq N$. Using (7), the auxiliary matrix $\boldsymbol{A} = (\boldsymbol{D} - \boldsymbol{I}) \cdot \boldsymbol{Y} \cdot \boldsymbol{Y^H}$ is described by its elements

$$a_{il} = \sum_{k=1}^{N} ((1+\epsilon_i)\cdot e^{j\cdot\xi_i} - 1)\cdot \delta[i-k]\cdot\ Y_k \cdot Y_l^* \quad (13)$$
$$a_{il} = ((1+\epsilon_i)\cdot e^{j\cdot\xi_i} - 1)\cdot\ Y_i \cdot Y_l^*.$$

where δ[.] is the discrete Kronecker delta.

Using this intermediate result, one may write the elements of $\boldsymbol{B} = (\boldsymbol{D}-\boldsymbol{I})\cdot\boldsymbol{Y}\cdot\boldsymbol{Y}^H\cdot(\boldsymbol{D}-\boldsymbol{I})^H$, the inner part of (12), as

$$b_{il} = \sum_{k=1}^{N} a_{ik}\cdot((1+\epsilon_i)\cdot e^{-j\cdot\xi_l} - 1)\cdot\delta[l-k]$$
$$b_{il} = a_{il}\cdot((1+\epsilon_l)\cdot e^{-j\cdot\xi_l} - 1) \quad (14)$$
$$b_{il} = (1+\epsilon_i)\cdot e^{j\cdot\xi_i} - 1)\cdot\ Y_i\cdot Y_l^*\cdot$$
$$((1+\epsilon_l)\cdot e^{-j\cdot\xi_l} - 1).$$

Taking the expectation using the independence assumptions [17] and the fact that, for the amplitudes $\epsilon_i \sim N(0,\sigma_\epsilon^2) \Rightarrow E[\epsilon_i]=0, E[\epsilon_i^2]=\sigma_\epsilon^2$ yields

$$E[b_{il}] = \{[1+E[\epsilon_i\cdot\epsilon_l]]\cdot E[e^{j\cdot(\xi_i-\xi_l)}] - E[e^{j\cdot\xi_i}] - E[e^{-j\cdot\xi_l}] + 1\}\cdot E[Y_i\cdot Y_l^*]$$
$$E[b_{il}] = \{E[e^{j\cdot\xi_i}]\cdot E[e^{-j\cdot\xi_l}] - E[e^{j\cdot\xi_i}] - E[e^{-j\cdot\xi_l}] + 1\}\cdot E[Y_i\cdot Y_l^*], \text{for } i\neq l \quad (15)$$
$$E[b_{ii}] = [\sigma_\epsilon^2 + 2\cdot E[1-\cos(\xi_i)]]\cdot E[Y_i\cdot Y_i^*], \text{for } i = l.$$

It can be shown by applying the theorem for the probability density of a function of a random variable [17] and direct integration that for $\xi \sim U\left(\frac{-\xi_u}{2},\frac{\xi_u}{2}\right)$

$$E[sin(\xi)] = 0,$$
$$E[cos(\xi)] = 2\cdot\frac{\sin\left(\frac{\xi_u}{2}\right)}{\xi_u} = sinc\left(\frac{\xi_u}{2}\right). \quad (16)$$

Hence, (15) becomes

$$E[b_{il}] = \left(1 - sinc\left(\frac{\theta_u}{2}\right)\right)^2\cdot E[Y_i\cdot Y_l^*], \text{for } i\neq l;$$
$$E[b_{ii}] = \left[\sigma_\epsilon^2 + 2\cdot\left(1-sinc\left(\frac{\theta_u}{2}\right)\right)\right]\cdot E[Y_i\cdot Y_i^*]. \quad (17)$$

At this point, it should be recalled that the cases of interest for the error assessment (residual calibration errors) involve relatively small values of ξ_u. For instance, if $\xi_u = 20°$, $1 - sinc\left(\frac{\xi_u}{2}\right) \cong 0.005$, meaning the matrix $\boldsymbol{B}$ is in practice quasi-diagonal. Moreover, the aliased signal covariance matrix is $\boldsymbol{R_{YY}} = E[\boldsymbol{Y}\cdot\boldsymbol{Y}^H] = \boldsymbol{H}\cdot E[\boldsymbol{S}\cdot\boldsymbol{S}^H]\cdot\boldsymbol{H}^H$, and since the signal components in the *N x 1* vector $\boldsymbol{S}$ represent non-overlapping azimuth *looks* of the Doppler SAR spectrum,

$$E[\boldsymbol{S}\cdot\boldsymbol{S}^H] = \text{diag}(\sigma_i{}^2)\ , 1\le i\le N. \quad (18)$$

Thus, $\boldsymbol{R_{YY}}$ has elements

$$r_{il} = E[Y_i\cdot Y_l^*] = \sum_{k=1}^{N}\sigma_k{}^2\cdot h_{ik}\cdot h_{lk}^*, \quad (19)$$

where h_{ik} are the entries of $\boldsymbol{H}$ (cf. (1)). In particular,

$$r_{ii} = E[Y_i\cdot Y_i^*] = \sum_{k=1}^{N}\sigma_k{}^2, \quad (20)$$

and (15) becomes

$$E[b_{il}] \cong \left[\sigma_\epsilon^2 + 2\cdot\left(1-sinc\left(\frac{\xi_u}{2}\right)\right)\right]\cdot\delta[i-l]\cdot\sum_{k=1}^{N}\sigma_k{}^2, \quad (21)$$

the approximation being that the off-diagonal terms are not exactly zero, but small for narrow error distributions.

Moreover, it can be recognized that the summation over $\sigma_k{}^2$ is the signal power $P_s = E[\boldsymbol{S}^H\cdot\boldsymbol{S}]$ summed over all azimuth *looks* for a given frequency f in I_1 (the omitted frequency dependency should be kept in mind).

Moving on with the calculation, one may note that, applying the property of the invariance of the trace to cyclic permutation of the matrix product

$$E[\|\boldsymbol{\Delta S}(f)\|^2] = tr\{E[\boldsymbol{\Delta S}(f)\cdot\boldsymbol{\Delta S^H}(f)]\} = tr\{\boldsymbol{P}\cdot E[\boldsymbol{B}]\cdot\boldsymbol{P}^H\} = tr\{\boldsymbol{P}^H\cdot\boldsymbol{P}\cdot E[\boldsymbol{B}]\}\ , \quad (22)$$

and from (21), the matrix $\boldsymbol{T} = \boldsymbol{P}^H\cdot\boldsymbol{P}\cdot E[\boldsymbol{B}]$ has elements

$$t_{il} = \left(\sum_{k=1}^{N} p_{ki}^*\cdot p_{kl}\right)\cdot\left[\sigma_\epsilon^2 + 2\cdot\left(1-sinc\left(\frac{\xi_u}{2}\right)\right)\right]\cdot P_S, \quad (23)$$

where p_{ik} denotes the entries of $\boldsymbol{P}$. Thus,

$$E[\|\boldsymbol{\Delta S}(f)\|^2] = tr\{\boldsymbol{T}\}$$
$$E[\|\boldsymbol{\Delta S}(f)\|^2] = \left[\sigma_\epsilon^2 + 2\cdot\left(1-sinc\left(\frac{\xi_u}{2}\right)\right)\right]\cdot P_S\cdot\left(\sum_{i=1}^{N}\sum_{k=1}^{N} p_{ki}^*\cdot p_{ki}\right)$$
$$E[\|\boldsymbol{\Delta S}(f)\|^2] = \left[\sigma_\epsilon^2 + 2\cdot\left(1-sinc\left(\frac{\xi_u}{2}\right)\right)\right]\cdot P_S\cdot\left(\sum_{i=1}^{N}\sum_{k=1}^{N} |p_{ki}|^2\right) \quad (24)$$
$$E[\|\boldsymbol{\Delta S}(f)\|^2] = \left[\sigma_\epsilon^2 + 2\cdot\left(1-sinc\left(\frac{\xi_u}{2}\right)\right)\right]\cdot P_S\cdot\|\boldsymbol{Q}\|^2,$$

where $\|\boldsymbol{Q}\|^2$ denotes the square of the Frobenius norm of the matrix $\boldsymbol{Q}$, formed by taking element-wise the absolute value of $\boldsymbol{P}(f)_{NxN}$. It is interesting to note that $\|\boldsymbol{Q}\|^2$ is closely related to the SNR scaling factor of the reconstruction, defined in [8] as

$$\Phi_{REC}(f_{PRF}) = N\cdot\sum_{k=1}^{N} E[|P_k(f)|^2]\ ,$$
$$\text{for } f \text{ in } [-N\cdot\frac{f_{PRF}}{2}, N\cdot\frac{f_{PRF}}{2}]$$
$$= \sum_{k=1}^{N}\sum_{m=1}^{N}|P_k(f+(m-1)\cdot f_{PRF})|^2 \quad (25)$$
$$= \sum_{k=1}^{N}\sum_{m=1}^{N}|P_{mk}(f)|^2\ , \text{for } f \text{ in } I_1.$$

They are in fact the same quantity $\|\boldsymbol{Q}\|^2 = \Phi_{REC}(f_{PRF})$, which even admits a closed-form analytical calculation following the strategy in [13], [16]. In (25) the expectation operator is understood to include an average over frequency of the deterministic quantities involved.

At this point, let the frequency dependency be restored, for clarity of interpretation, and an average over frequency be introduced as

$$P_{amb} = \frac{1}{f_{PRF}} \cdot \int_{-N\cdot\frac{f_{PRF}}{2}}^{-N\cdot\frac{f_{PRF}}{2}+f_{PRF}} E[\|\boldsymbol{\Delta S}(f)\|^2] \cdot df$$

$$P_{amb} = \left[\sigma_\epsilon^2 + 2 \cdot \left(1 - sinc\left(\frac{\xi_u}{2}\right)\right)\right] \cdot \frac{1}{f_{PRF}} \cdot \int_{-N\cdot\frac{f_{PRF}}{2}}^{-N\cdot\frac{f_{PRF}}{2}+f_{PRF}} \left(\sum_{i=1}^{N}\sum_{\boldsymbol{k=1}}^{\boldsymbol{N}} |p_{ki}|^2\right) \cdot P_S(f) \cdot df \quad (26)$$

$$P_{amb} = \left[\sigma_\epsilon^2 + 2 \cdot \left(1 - sinc\left(\frac{\xi_u}{2}\right)\right)\right] \cdot \|\boldsymbol{Q}\|^2 \cdot P_{signal}^{avg},$$

where P_{signal}^{avg} is the average signal power over all frequencies in I_1.

Using this result, one may define the error induced AASR as

$$AASR_{errors} = \frac{P_{amb}}{P_{signal}^{avg}}$$

$$AASR_{errors} = \left[\sigma_\epsilon^2 + 2 \cdot \left(1 - sinc\left(\frac{\xi_u}{2}\right)\right)\right] \cdot \left(\sum_{i=1}^{N}\sum_{\boldsymbol{k=1}}^{\boldsymbol{N}} |p_{ki}|^2\right) \quad (27)$$

$$AASR_{errors} = \left[\sigma_\epsilon^2 + 2 \cdot \left(1 - sinc\left(\frac{\xi_u}{2}\right)\right)\right] \cdot \|\boldsymbol{Q}\|^2,$$

which is the final and main result of this section. It is interesting to note that the SNR scaling factor also effectively scales the ambiguous energy due to residual channel imbalances, which is a new result following from the presented derivation.

3. Simulation Results

In the following, the analytical AASR model is verified by means of a Monte Carlo simulation of a C-Band multichannel SAR system. The reconstruction of a point target at a look angle θ_{look}= 21.85° is performed for 256 realizations of the errors drawn from the appropriate distributions (i.e. $U\left[-\frac{\xi_u}{2}, \frac{\xi_u}{2}\right]$ for phase errors and $N(0, \sigma_\epsilon^2)$ for amplitude errors) and the average AASR (estimated for each realization using the impulse response based method of [18]) is taken as an estimation of the expected values. This is repeated for different values of the corresponding error distribution parameters (ξ_u or σ_ϵ^2) to measure the performance degradation as a function of the error magnitude for each kind of error. The phase and amplitude errors are analyzed independently to allow a better visualization of the results, and the simulated signals are noiseless. Given the relevance of the noise scaling factor $\|\boldsymbol{Q}\|^2$ for the sensitivity with respect to errors (cf. (27)), two different scenarios corresponding to two different values of f_{PRF} are considered, in order to illustrate the behavior both for favorable and unfavorable sampling conditions. In the former case, $AASR_{error-free}$ is low and $\|\boldsymbol{Q}\|^2 \cong 1$, whereas in the latter both quantities are higher. The system parameters are summarized in Table 1.

Relevant System Parameters (Azimuth)

Quantity	Symbol	Value
Orbit height	h_{orbit}	745 km
Wavelength	λ	5.54 cm
Antenna length in azimuth	l_{az}	12.8 m
Number of azimuth channels	N_{az}	16
(Physical) Spacing of azimuth channels	Δx_{az}	0.8 m
Processed Bandwidth	Bw_{proc}	7505 Hz
Goal azimuth resolution	δ_{az}	1 m

Table 1: Simulation Scenario Parameters

The first scenario regards a $f_{PRF} = 1245$ Hz, higher than the uniform PRF of 1172.5 Hz, and presents a multichannel PRF of $N \cdot f_{PRF} = 19920$ Hz. This means considerable oversampling with respect to the signal bandwidth, and hence the band-limitation assumption for the signal virtually holds. As expected, error-free reconstruction leads to a very low AASR of -77 dB, whereas achieving an azimuth resolution of 0.8 m. The corresponding impulse response is depicted in Figure 2 (a). The ambiguities at integer multiples of f_{PRF}, highlighted in blue, show very low levels. In contrast, they are visibly higher in Figure 2 (b), which is the result of reconstruction with channels affected by (a realization of) phase errors drawn from an uniform distribution in the interval [-5°, 5°] (i.e., ξ_u = 10°).

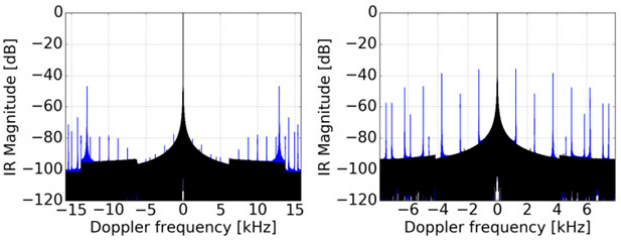

(a) (b)

Figure 2: Example of reconstruction with and without channel imbalances for the first scenario ($f_{PRF} = 1245$ Hz). (a) shows the impulse response for error-free reconstruction, with very low AASR. The ambiguities are highlighted in blue. (b) shows the impulse response for the reconstruction with a realization of uniform phase errors drawn from the interval [-5°, 5°], causing a visible increase in the ambiguity level.

Figure 3 (a) and (b) illustrate the histograms of the AASR over the Monte Carlo trials, respectively for varying ξ_u (phase errors) and σ_ϵ. The expected value of the AASR for each value of the respective distribution parameter is highlighted by vertical dashed lines in the same color of the histograms. It is clear that the AASR rises quickly from the error-free value for small errors, but the histograms migrate more slowly towards larger AASR levels for higher error magnitudes.

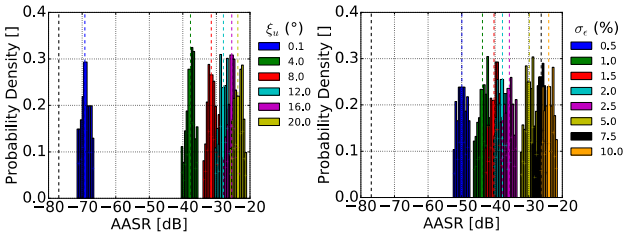

(a) (b)

Figure 3: Monte Carlo simulation of reconstruction in the first scenario ($f_{PRF} = 1245$ Hz). (a) shows the histograms of the AASR of the Monte Carlo trials for example values of the phase error distribution parameter ξ_u. (b) shows the histograms of the AASR of the Monte Carlo trials for example values of the amplitude error distribution parameter σ_ϵ. In both plots, the black vertical dashed line indicates the error-free AASR level and the color coded vertical dashed lines indicate the mean of each histogram.

The second scenario was designed to achieve error-free AASR levels of -25 dB. The degraded performance is obtained by reducing the PRF up to $f_{PRF} = 1090$ Hz, which does not change the achieved resolution.

The AASR induced by phase and amplitude errors, as estimated by the Monte Carlo approach, is shown as a function of the distribution parameters ξ_u and σ_ϵ in Figure 4, for both f_{PRF} scenarios. The center of the error bars correspond to the position of the vertical dashed lines in Figure 3. Their extent marks one standard deviation to each side of the mean over the Monte Carlo trials, for a particular value of ξ_u or σ_ϵ.

The analytical model prediction calculated from (11), (27) is also plotted, showing good agreement to the Monte Carlo simulations, especially for smaller errors. The maximum deviation between the curves is overall smaller than 0.5 dB. The AASR levels vary strongly for small errors due to the very low initial values of the first scenario (as can also be seen from the histograms in (a) and (b)), but as expected show saturation effects and a reduced sensitivity for larger imbalances, as well as for larger initial error-free AASR (cf. Figure 4 (c), (d)). The level of -25 dB, considered a threshold of the maximum acceptable residual ambiguity limit, is reached for $\xi_u \cong 16°$ or $\sigma_\epsilon \cong 8\%$ in the first f_{PRF} scenario.

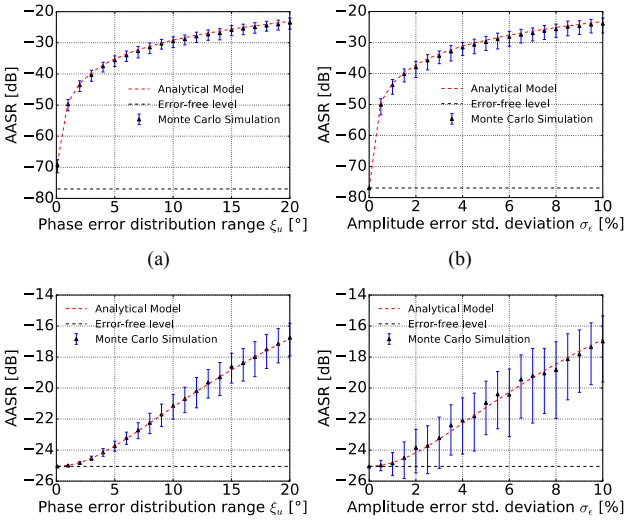

(a) (b) (c) (d)

Figure 4: AASR as function of phase error uniform distribution range ξ_u (a, c) and amplitude error standard deviation σ_ϵ (b, d), for $f_{PRF} = 1245$ Hz (a, b) and $f_{PRF} = 1090$ Hz (c, d). The blue dots show the average derived from the Monte Carlo simulations, whereas the error bar shows an interval of one standard deviation to each side of the mean. The red dashed line shows the result of the analytical prediction, with the error-free level (respectively -77 and -25 dB for the two scenarios) indicated by a horizontal black dashed line.

Finally, to illustrate the usefulness of the presented derivation in deriving requirements, a mapping of the total AASR (with errors) as a function of the initial error-free AASR and the phase error distribution range ξ_u is shown in Figure 5. In this example, $\|\boldsymbol{Q}\|^2$=1, meaning uniform sampling is considered, and no amplitude errors occur ($\sigma_\epsilon^2 = 0$), which can be understood as a best-case analysis of the behavior of the phase-error induced AASR. The contour lines of the total AASR illustrate how a trade-off between the maximum residual phase error (which translates into calibration requirements) and the sampling conditions (a function of element spacing and PRF) may be used to achieve a specified performance level in the system design. The results illustrate on the one hand that the error contribution quickly dominates for operating points in which the error-free level is very low, making them hardly achievable in practice. On the other hand, some margin for the error contribution is seen to be required, according to the hardware's and calibration system capabilities in terms of the achievable residual error magnitude.

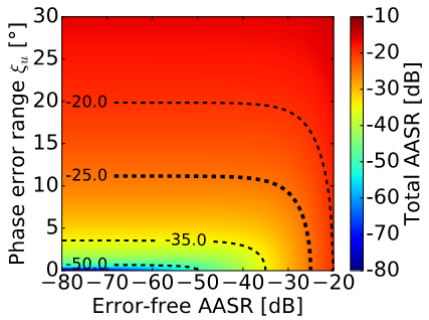

Figure 5: 2D mapping of total AASR as a function of the error-free AASR (abscissa) and the phase error distribution parameter ξ_u (ordinate), with contour lines indicating total AASR level boundaries in dB**.**

4. Final Remarks and Discussion

The paper presented a residual phase-amplitude error model for a system with multiple receive channels in azimuth and derived mathematically an analytical model for the error's impact on the ambiguous energy found in the reconstructed image, measured by means of the AASR performance parameter. An interesting new result is that the well-known SNR scaling parameter also plays an important role in the scaling of the error-induced ambiguous energy. The sampling conditions are therefore also relevant for the robustness of the processing approach with respect to errors in the channel's transfer functions.

The model was validated to a good extent by means of Monte Carlo simulations of the errors, following the appropriate probability distribution assumed in the derivation. This leads to the conclusion that the assumed approximations are reasonable and no appreciable deviations are expected from the more computationally costly Monte Carlo approach. The model thus presents itself as a simple and effective alternative to estimate the impacts of residual errors and may be used as a design-aid for e.g. establishing calibration requirements.

References

[1] J. C. Curlander and R. N. McDonough. "Synthetic Aperture Radar: Systems and Signal Processing", New York: Wiley, (1991).

[2] A. Moreira, P. Prats-Iraola, M. Younis, G. Krieger, I. Hajnsek and K. P. Papathanassiou, "A tutorial on synthetic aperture radar," in *IEEE Geoscience and Remote Sensing Magazine*, **vol. 1**, no. 1, pp. 6-43, (2013).

[3] G. Krieger *et al.*, "SIMO and MIMO System Architectures and Modes for High-Resolution Ultra-Wide-Swath SAR Imaging," in *11th European Conference on Synthetic Aperture Radar (EUSAR)*, pp. 1-6., Hamburg, (2016).

[4] M. Younis et al., "Techniques and Modes for Multi-Channel SAR Instruments," in *11th European Conference on Synthetic Aperture Radar (EUSAR)*, pp. 1-6, Hamburg, (2016).

[5] A. Freeman et al., "The "Myth" of the minimum SAR antenna area constraint," *IEEE Transactions on Geoscience and Remote Sensing*, **vol. 38**, no. 1, pp. 320-324, (2000).

[6] G. Krieger, N. Gebert and A. Moreira, "Unambiguous SAR signal reconstruction from nonuniform displaced phase center sampling," in *IEEE Geoscience and Remote Sensing Letters*, **vol. 1**, no. 4, pp. 260-264, (2004).

[7] G. Krieger, N. Gebert and A. Moreira. "Multidimensional Waveform Encoding: A New Digital Beamforming Technique for Synthetic Aperture Radar Remote Sensing", *IEEE Transactions on Geoscience and Remote Sensing*, **vol. 46**, no. 1, pp.31-46, (2008).

[8] N. Gebert, G. Krieger, and A. Moreira. "Digital beamforming on receive: Techniques and optimization strategies for high resolution wide-swath SAR imaging", *IEEE Transactions on Aerospace and Electronic Systems*, **vol. 45**, pp. 564–592, (2009).

[9] G. Adamiuk, C. Schaefer, C. Fischer and C. Heer. "SAR Architectures based on DBF for C- and X-band applications", *10th European Conference on Synthetic Aperture Radar (EUSAR)*, pp. 1-4, (2014).

[10] A. Papoulis, "Generalized Sampling Expansion", *IEEE Transactions on Circuits and Systems*, **vol. 24**, no. 11, pp. 652-654, (1977).

[11] J. L. Brown, "Multi-Channel Sampling of Low-Pass Signals", *IEEE Transactions on Circuits and Systems*, **vol. 28**, no. 2, pp. 101-106, (1981).

[12] N. Gebert, F. Queiroz de Almeida, and G. Krieger. "Airborne demonstration of multichannel SAR imaging", *IEEE Geoscience and Remote Sensing Letters*, **vol. 8**, no. 5, pp. 963–967, (2011).

[13] D. Seidner and M. Feder. "Vector Sampling Expansion", *IEEE Transactions on Signal Processing*, **vol. 48**, no. 5, pp. 1401–1416, (2000).

[14] I. Sikaneta, C.H. Gierull, and D. Cerutti-Maori. "Optimum signal processing for multichannel SAR: with application to high-resolution wide-swath imaging", *IEEE Transactions on Geoscience and Remote Sensing*, **vol. 52**, no. 10, pp. 6095–6109, (2014).

[15] D. Cerutti-Maori, I. Sikaneta, J. Klare and C. H. Gierull, "MIMO SAR Processing for Multichannel High-Resolution Wide-Swath Radars," in *IEEE Transactions on Geoscience and Remote Sensing*, **vol. 52**, no. 8, pp. 5034-5055, (2014).

[16] D. Seidner and M. Feder. "Noise amplification of periodic nonuniform sampling", *IEEE Transactions on Signal Processing*, **vol. 48**, no. 1, pp. 275–277, (2000).

[17] A. Papoulis and S. U. Pillai. "Probability, random variables, and stochastic processes", Chapter 5, New York: McGraw Hill, (2002).

[18] M. Villano, G. Krieger and A. Moreira "Ambiguities and image quality in staggered SAR" in 5th Asia-Pacific Conference on Synthetic Aperture Radar (APSAR), Singapore, pp. 204-209, (2015).